# Design and Control of Micro-actuators for High Density Disk Drives

by

**Sanjay K. Aggarwal**

Supervisor: Professor R. Horowitz

Submitted in partial satisfaction of the
requirements for the degree of

Master of Science

in

Mechanical Engineering

in the

GRADUATE DIVISION

of the

UNIVERSITY of CALIFORNIA at BERKELEY

May 1997

## ABSTRACT

A brief discussion of a previously designed parallel plate micro-actuator is provided. Theoretical models for the parallel plate design are then developed to motivate models used in the control design and to illustrtate non-linear effects of the parallel plate design. Electrostatic simulations are performed for a comb finger, high aspect ratio micro-actuator geometry to illustate non-linear effects in an alternative design approach. These simulations show a significant amount of non-linearity in comb fingers under certain operating conditions, though they also show the geometries neccesary for linear operation.

Initial continuous-time control designs for the dual-stage servo have been designed and simulated using Matlab's μ-tools. Single-input/single-output (SISO) and multi-input/multi-output (MIMO) control design methods have been shown to be capable of meeting specified uncertainty and performance specifications. Uncertainty models have included bearing effects in the disk drive arm as well as high frequency dynamics not included in the system model. Simulations using a linearized system model with the SISO design achieved a low frequency disturbance rejection of 59 dB with a bandwidth of 2.0 kHz. The MIMO design also achieved a low frequency disturbance rejection of 59 dB with a bandwidth of 3.0 kHz. The μ-tools design procedure and software for both design methods is also described.

## ACKNOWLEDGEMENTS

I extend my sincere thanks to Professor Roberto Horowitz for his help and support throughout my master's research. His time and care in discussing my research was truly appreciated. I also thank Professor Andy Packard for all of his help in using μ-tools. His instruction and advice was invaluable throughout my research.

To everyone in the CML Servo Lab, I enjoyed working with all of you. I particularly thank Dave Horsley and Satinderpall Pannu. Dave was always a great source of ideas and help with my design work on the micro-actuator, and I really thank him for all of the research material and slides he let me use in this report and in my presentation. Sat was just someone I could always count on for anything I needed. You both were good friends, and I am sure I'll see a lot of you even after I start working.

# CHAPTER 1

# Background

## 1.1 Introduction

Increases in data storage density in magnetic disk drives have necessitated the development of increasingly higher performance servo systems. At the current annual rate of increase of 60%, data densities are expected to reach 10 GBit/in$^2$ by the turn of the century [1]. This translates into a linear track density of 25,000 tracks per inch, or a track width of 1 μm. The predicted servo requirements corresponding to these specifications are a bandwidth near 2 kHz, and a tracking accuracy near 100 nm [2][3]. Conventional servo actuators cannot achieve this high bandwidth or provide this level of tracking accuracy due to resonances in the positioning arm and low frequency bearing effects. Thus, the use of a micro-actuator as a secondary positioning mechanism for high-bandwidth, high accuracy control was proposed [4]. Current piezoelectric actuators built for this task do not use direct position measurements from the micro-actuator and thus cannot achieve sufficient positioning accuracies [5]. Previous microfabricated electrostatic devices have been too small to provide an adequate output force [4][6]. Recently, high aspect ratio batch-fabricated devices, which produce sufficient force to move the slider with the required bandwidth, have been fabricated both from polysilicon [7] and from electroplated metal [2][8]. In this paper, we discuss the design of the polysilicon actuators as well as the servo system for this new generation of high aspect ratio actuators.

### 1.1.1 Dual-Stage Disk Drive

A schematic of a conventional disk drive is shown in Figure 1.1. The positioning system consists of a sin-

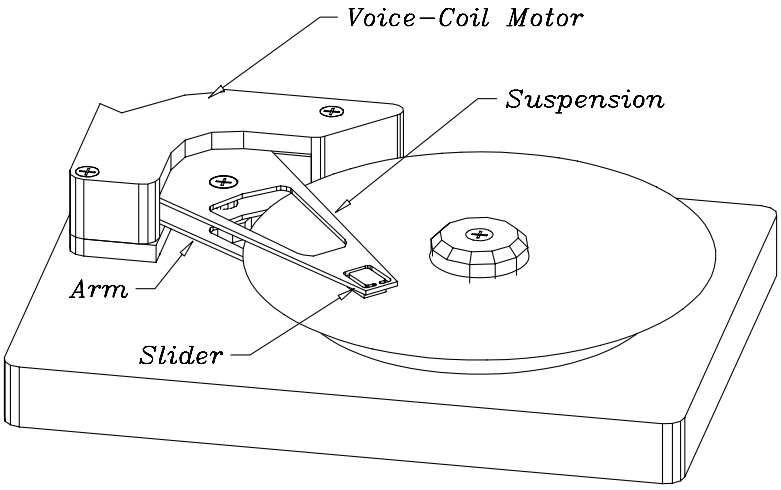


***Figure 1.1*** *Schematic of conventional single-stage disk drive.*

gle suspension mounted on an arm, which is actuated by an electromagnetic voice coil motor (VCM). The arm plus suspension (herein just referred to as the arm) sweep a ceramic slider radially across the disk surface, allowing the read/write elements to transfer data to the disk. The only position measurement is the position error signal (PES), which is read off of the disk by the read/write head and measures the head deviation from the track center.

To circumvent the limitations of a single-stage positioning system, the dual-stage actuator schematically

shown in Figure 1.2 is proposed in this paper. In this system, the micro-actuator, which is sandwiched between the slider and the gimbal at the end of the arm, rotates the slider relative to the gimbal and acts as a fine-positioning mechanism while the arm continues to perform coarse-positioning. Thus, the micro-actuator will only be used to follow a single data track, and track seeking will continue to be performed by the arm alone. The micro-actuator will also be a high-bandwidth device, as is necessary for achieving higher data densities, and will be fabricated so as not to suffer from the frictional effects experienced by the arm. Position measurements from the micro-actuator will be used in the servo loop to achieve the desired bandwidth and accuracy.

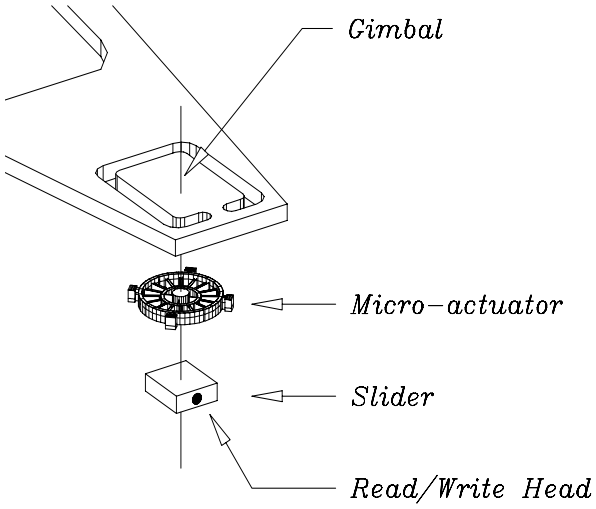


***Figure 1.2*** *Exploded view of micro-actuator assembly. The micro-actuator is sandwiched between the slider and the gimbal at the end of the arm.*

# CHAPTER 2

# Micro-actuator Design

## 2.1 Overview

The micro-actuator to be used in the dual-stage disk drive is intended to be a polysilicon, electrostatic, high aspect ratio device. An electrostatic means of actuation was chosen for its potential to produce a high output force with a relatively small amount of power dissipation. Though an electrostatic device may require a high output voltage, the currents needed to drive the actuator tend to be small. High aspect ratio geometries were chosen to increase the force output and sensing signal to noise ratio. These high aspect ratio devices have become recently become more feasible due to advances in fabrications technologies for micro-electro-mechanical devices.

Two possible actuator geometries have been investigated thus far. The first uses parallel capacitive plates to drive the actuator, and the second uses inter-digitated comb fingers. The initial micro-actuator designed and fabricated by David Horsley uses the parallel plate geometry. A brief description of Horsley's design is presented here along with the theoretical model used for parallel plate geometries. Electrostatic simulations for comb finger geometries are also presented below. These simulations help provide design optimization guidelines for future micro-actuator designs.

## 2.2 Parallel Plate Micro-Actuator Design

Horsley fabricated parallel plate, polysilicon, electrostatic micro-actuators using the HexSil process [9]. Complete details on the design and fabrication of these devices are contained in [7]. Figure 2.1 shows an

SEM of a completed actuator. The device consists of pairs of capacitive plates which attach to a rotating inner ring (or rotor) and a fixed outer ring (or stator). The capacitive plates have a nominal gap size of 11 μm and will be used to actuate the device as well as to obtain position measurements from the actuator using a capacitive sensing scheme [6]. The rotor is attached to an anchored central column via 4 μm wide, 100 μm tall flexures. These high aspect ratio (25:1) flexures allow the device to have a low resonant frequency about the controlled yaw axis, while maintaining high stiffness about other axes. Thus, a single, well-defined resonance affects the control design. Furthermore, the use of flexures avoids the bearing friction limitations of the arm. The finished actuators are 100 μm thick and 2.6 mm in diameter, which is slightly larger than the 1.2 mm x 1 mm footprint of a standard pico-slider. Since the micro-actuator is only expected to move the slider ±1 μm, the maximum angular rotation of the micro-actuator is then 2 mrad.

A rotational topology was chosen for the actuator to allow for a high linear acceleration at the tip of the slider, where the read/write head is located, while avoiding acceleration of the center of mass of the slider. Additionally, the design should prove to be extremely robust to linear shock disturbances to the drive.

### 2.2.1 HexSil Fabrication Process

The HexSil fabrication process [9] allows for the low-cost batch production of high aspect-ratio polysili-

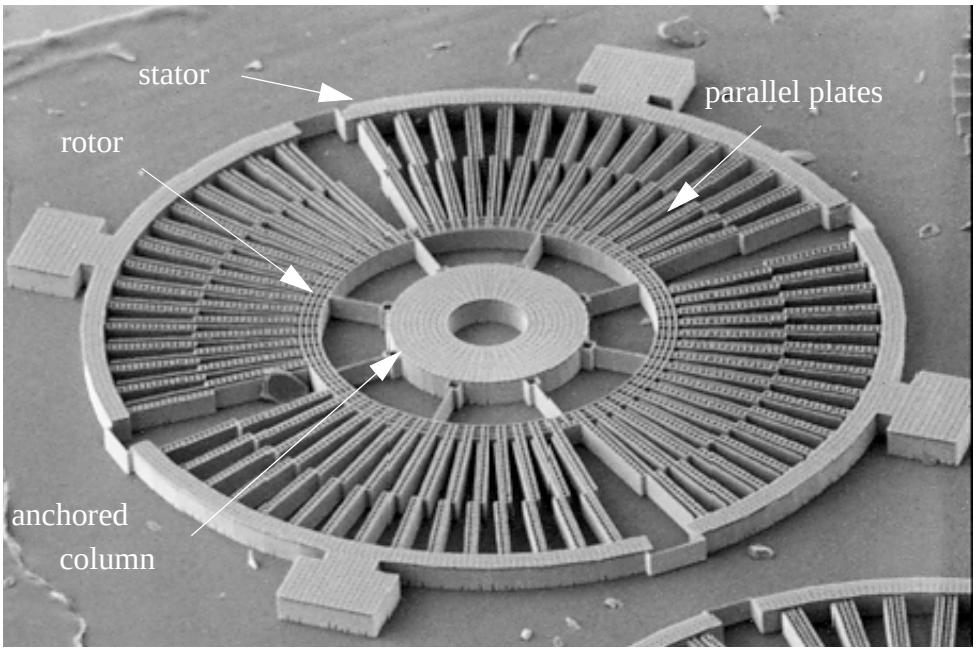


***Figure 2.1*** *SEM of 100 μm high, 2.6 mm diameter micro-actuator.*

con structures. In electrostatic actuators, the aspect ratio is critical because the output torque and position sensing signal to noise ratio increase linearly with aspect ratio for a given capacitive gap. Additionally, for a fixed yaw axis rotational stiffness, the flexural stiffness of the actuator about the pitch and roll axes increases quadratically with the aspect ratio. The structures are fabricated by depositing polysilicon into re-usable molds formed in silicon wafers, then released from the molds and transferred to target substrates using a solder bond [10]. In addition to allowing the integration of micro scale structures with macroscopic mechanical parts such as the disk-drive suspension, the process provides the ability to transfer actuators onto standard CMOS dice containing position sensing and high voltage driving electronics.

### 2.2.2 Electrostatic Actuation

The actuator consists of N pairs of capacitive plates, half of which are used for clockwise rotation, and half for counter-clockwise rotation. For small rotation angles, θ, the plates can be considered as parallel plate capacitors with gaps $x_1$ and $x_2$:

$$x_1 = x_n - r\theta \quad x_2 = x_n + r\theta \ , \tag{2.1}$$

where r is the distance from the center of the rotor to the center of the plate, and $x_n$ is the nominal plate gap. Applying voltage $v_1$ to one half of the structure results in an electrostatic torque

$$\tau(v_1, \theta) = \frac{N}{4} r\varepsilon_o A\left(\frac{v_1}{x_1}\right)^2 = \frac{N}{4} r\varepsilon_o A\left(\frac{v_1}{x_n - r\theta}\right)^2 \ , \tag{2.2}$$

where $A$ is the plate area and $\varepsilon_o$ is the permittivity of air. As seen in Eq. (2.2), the output torque is a non-linear function of both voltage and rotation, θ. The voltage non-linearity may be reduced by applying differential voltages $v_1$ and $v_2$ to the two halves of the structure, where

$$v_1 = v_b + v_c \qquad v_2 = v_b - v_c \ . \tag{2.3}$$

Here $v_b$ is a fixed DC bias and $v_c$ is the control voltage.

The effect of this differential driving scheme is shown in Figure 2.2 (figure from static tests performed by

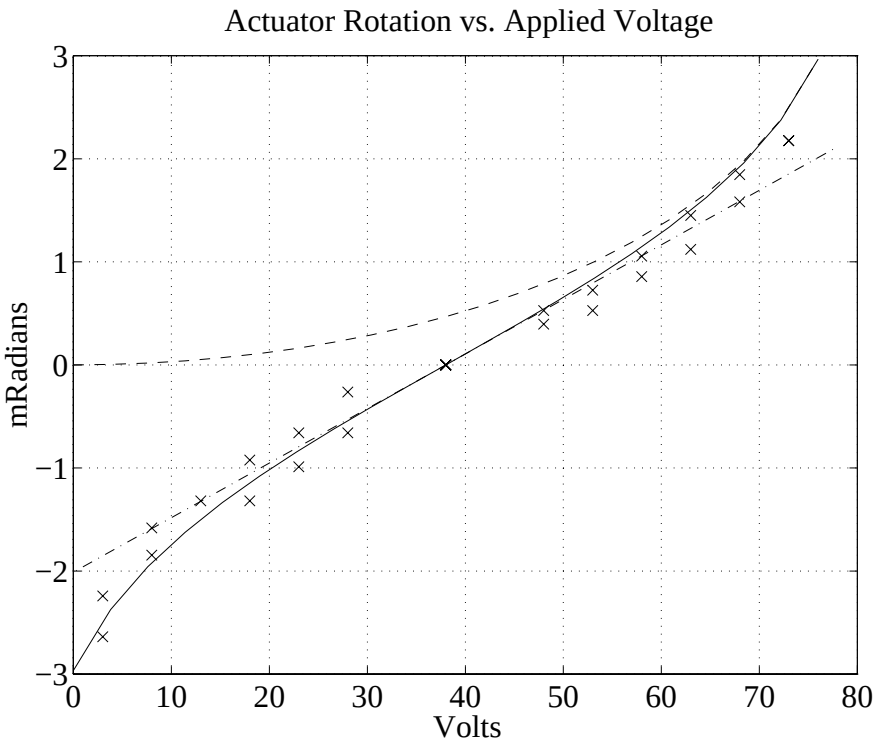


***Figure 2.2*** *Actuator rotation vs. applied voltage. The dashed line shows the rotation when only one-half of the structure is driven, while the solid line shows the rotation produced when both halves are used in a differential configuration. An x indicates an experimental data point. The dash-dot line is the linearized model.*

Horsley). For a constant control voltage, $v_c$, the actuator rotation is given by

$$\theta(v_c) = \frac{\tau(v_1, \theta) - \tau(v_2, \theta)}{K_\theta}, \tag{2.4}$$

where $K_\theta$ represents the mechanical spring stiffness of the flexures which couple the rotor to the fixed anchor, and $\tau(v_1,\theta)$ and $\tau(v_2,\theta)$ are given by Eq. (2.2). The plot shows the rotation predicted by Eq. (2.2) and the resultant rotation produced by the differential drive relationship expressed in Eq. (2.4). On the plot, an 'x' indicates the measured rotation of a 30 μm tall version of the actuator under an applied DC bias of $v_b$ = 38 V and a control voltage, $v_c$, between ±35 V. Note that the relationship between voltage and rotation is approximately linear for rotations less than ±1.5 mrad, as seen from the dash-dot line representing the linearized model described below. Notice that the micro-actuator is not expected to rotate more than 2 mrad.

### 2.2.3 Dynamic Model

For small rotational angles, the output torque can be approximated by a linearized model

$$\tau(v_c, \theta) = k_v v_c + k_e \theta \ . \tag{2.5}$$

Here $k_e$ is a destabilizing electrical spring stiffness, which is given by

$$k_e = \frac{\partial}{\partial \theta}\tau(v_c, \theta)\Big|_{(0,\,0)} = \frac{Nr^2 \varepsilon_o A v_b^2}{x_n^3} \ , \tag{2.6}$$

and $k_v$ is the voltage to torque gain, given by

$$k_v = \frac{\partial}{\partial v_c}\tau(v_c, \theta)\Big|_{(0,\,0)} = \frac{Nr\varepsilon_o A v_b}{x_n^2} \ . \tag{2.7}$$

The overall second order dynamic equation for the micro-actuator is then

$$I\ddot{\theta} + b\dot{\theta} + (K_\theta - k_e)\theta = k_v v_c \ , \tag{2.8}$$

where $I$ is the combined inertia of the micro-actuator and slider and $b$ is the damping coefficient. Open loop stability is assured for $K_\theta > k_e$ .

### 2.2.4 Actuator Results

The actuator is designed to carry a pico-slider and operate from an 80 V supply. A high voltage CMOS charge pump circuit is being designed which will be located adjacent to the micro-actuator and will provide the drive voltage by amplifying a base voltage on the order of a few volts, depending on the specific application. Due to the nature of electrostatic actuation, currents in the nanoamp range will be necessary, and thus very little power will actually be required to drive the micro-actuator. Given that the pico slider has a moment of inertia of 0.36 mg-mm$^2$, the actuator must provide a minimum torque of at least 0.19 mN-mm to provide a range ±1 μm over a bandwidth of 2 kHz. Under the differential driving scheme given by

Eq. (2.3), with a DC bias of 40 V and a maximum control voltage swing of ±40 V, the DC gain from voltage to position is 64 μrad/V. This gain is indicated in Figure 2.2 by the slope of the dash-dot line. Note that the actuator must rotate ±2 mrad to provide a ±1 μm displacement at the read/write elements of the slider, requiring a voltage to position gain of at least 50 μrad/V. The open loop bandwidth of the actuator is therefore defined as the maximum frequency at which this gain is achieved. Including a pico-slider payload and assuming critical damping as a pessimistic estimate, the calculated actuator natural frequency is 1.8 kHz, and the required voltage gain can be achieved out to a maximum bandwidth of approximately 1.6 kHz. All other actuator parameters can be found in [7].

## 2.3 Comb Finger Simulations

An alternative to the parallel plate actuator geometry discussed above is the use interdigitated comb fingers. As seen in Eq. (2.2), the torque created by the parallel plate device is inversely proportional to $x^2$. Even with a differential driving scheme, this non-linearity can potentially degrade the performance of the micro-actuator if not properly accounted for. Although the results shown in Figure 2.2 contain a fairly small amount of non-linearity over the desired range of motion, future parallel plate designs may exhibit more non-linearity. Once the actuator diameter is decreased to conform to the size of the slider, the nominal gap between the plates may also need to be reduced to maintain the same torque output; the result would be greater force non-linearity. With the comb finger geometry, the force is expected to be independent of $x$, and thus the torque nonlinearity should be less of a concern. In order to verify the range of linear operation for high aspect ratio comb finger geometries, electrostatic simulations for various high aspect ratio comb finger geometries were performed using a boundary element software developed by Per Ljung, a student at UC Berkeley.

A schematic of the finger geometry used in the simulations is shown in Figure 2.3. The direction of actuation is along $x$. The lower finger is fixed to a ground plane and the other is 2 units (all units normalized) above the ground plane at a potential of 1 V. Due to the symmetry of the comb finger layout, only a half cell of a finger was necessary to perform the simulation. A full cell contains a mirrored version of the half cell shown, and a full actuator layout contains repeated versions of the full cell. In the simulations, the parameters labeled in the figure were each independently varied. For each combination of parameters, the capacitance between the two fingers was determined as the amount of overlap of the fingers was varied. The force on the fingers was then calculated by fitting a curve to the capacitance data and taking the deriv-

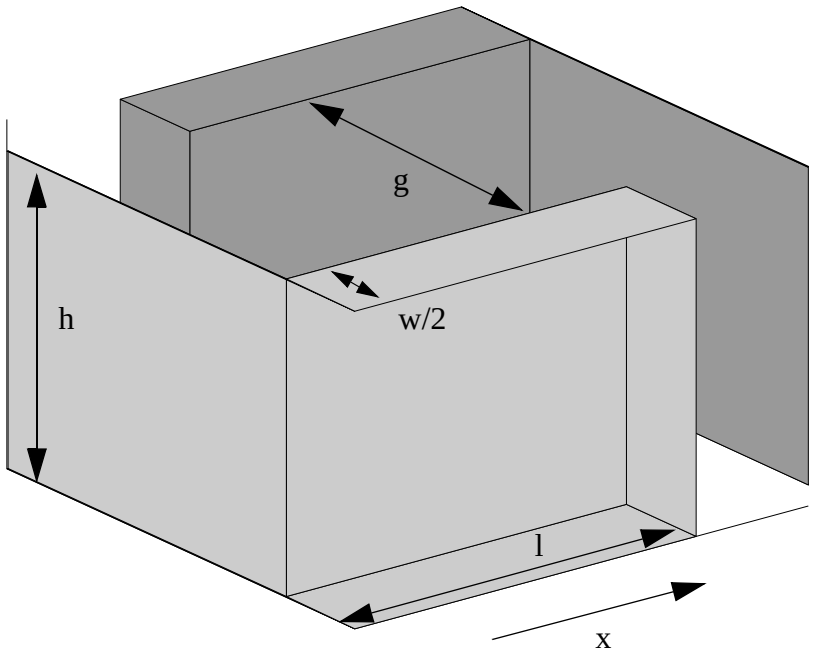


***Figure 2.3*** *Schematic of comb finger half cell used for electrostatic simulations.*

ative of the capacitance with respect to *x*. This analysis used all normalized parameter values and did not include the physical constants relating the derivative of the capacitance to the force.

The curve fit obtained from the simulations for the capacitance between the fingers is

$$C_{fit} = \left[\frac{h}{g} - 2.5\right]x + \frac{h[w + 0.25g] + 12}{(l - x)} + Const \quad x = fingeroverlap \quad . \tag{2.9}$$

Each of the terms in Eq. (2.9) corresponds to the capacitance due to a different part of the finger. The first term, which is linear in *x*, is due to the capacitance between the two faces which are separated by the distance *g*. This term creates a force independent of *x*. As expected for a parallel plate capacitor, the capacitance roughly corresponds to the area of overlap of the two faces divided by the separation of the faces. The extra factor of 2.5 is due to nonlinear effects. The second term corresponds to the capacitance at the tips of the fingers. This term again roughly corresponds to the area of the tip face divided by the separation of the faces. The final term is a constant independent of *x* and is due to the capacitance between the

finger and a ground plane. This constant varies for different finger geometries. However, a fit was not determined because this term does not affect the force on the finger.

The results from taking the derivative of the curve fit in Eq. (2.9) is shown in Figure 2.4. The plots shown correspond to the finger parameters for which capacitance simulations were actually performed. The key feature to note is that although the force is expected to be independent of *x*, a significant amount of nonlinearity appears as the finger overlap approaches the finger length, and thus the fingers are almost completely engaged. This results from the capacitance at the tips of the fingers. As the fingers become almost completely disengaged, the force approaches the expected constant value. Using these simulation results, an actuator utilizing a comb finger geometry can be designed to minimize the effect of non-linearities and potentially simplify implementation of the micro-actuator.

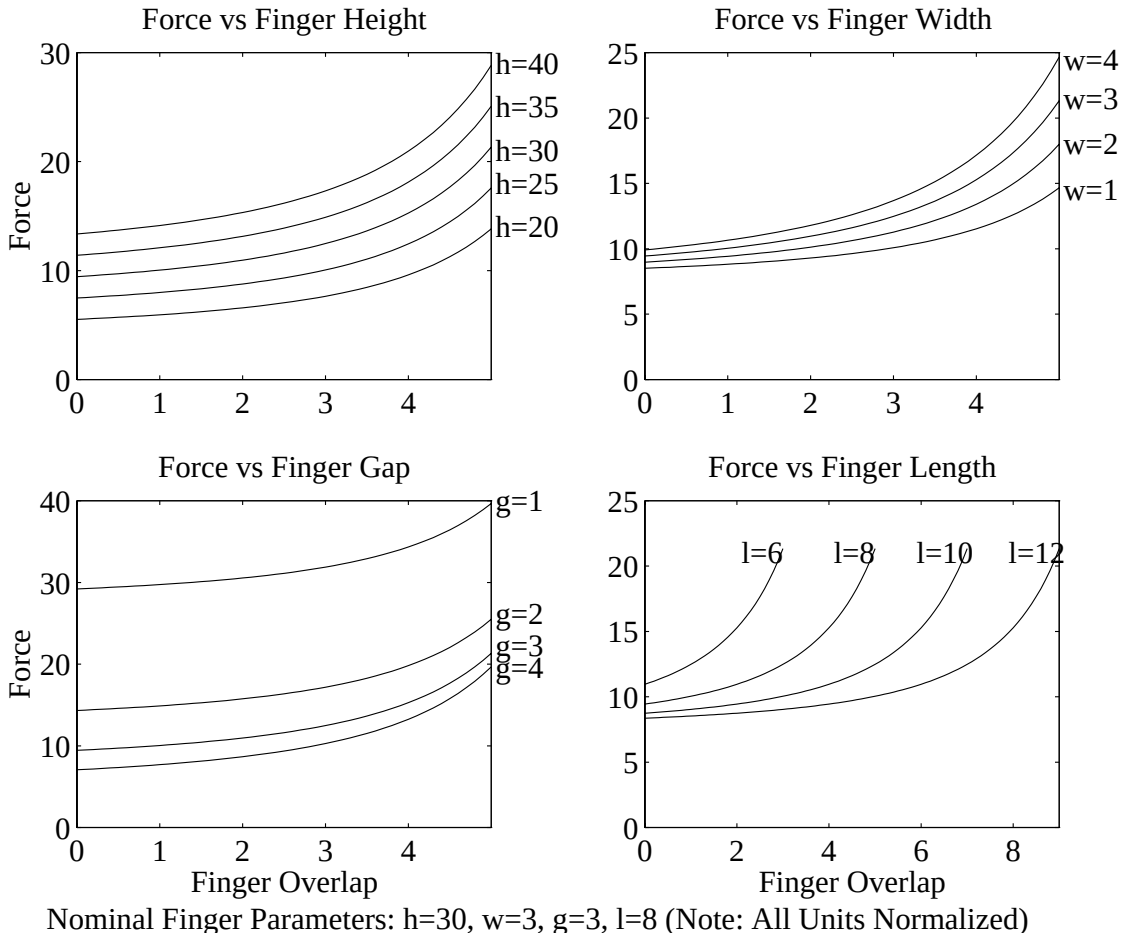


***Figure 2.4*** *Electrostatic simulation results for high aspect ratio comb fingers.*

# CHAPTER 3

# Control Design

## 3.1 Overview

The use of a secondary positioning mechanism in a disk drive requires the development of a more sophisticated controller than is required in a conventional drive. During track seek, the micro-actuator is inactive, and conventional track seek control algorithms can be used. During the track following mode, however, the micro-actuator is active, and the new controller can use measurements of the PES and the micro-actuator position relative to the arm to attempt to keep the PES within its allowable limits while still maintaining the micro-actuator within its range of motion. At low frequencies where disturbances tend to be large, tracking must be done primarily by the arm, with the micro-actuator performing some fine-positioning to compensate for frictional limitations in positioning the arm. At higher frequencies, where disturbances are smaller and resonances limit the capabilities of the arm, the micro-actuator performs tracking. This chapter discusses the control methodologies possible for the dual-stage servo design as well as the specific controller requirements and the resulting controller simulation results.

## 3.2 Control Design

Two continuous-time control design approaches have been investigated, each designed using Matlab's μ-tools toolbox. The first is a single-input/single-output (SISO) approach which assumes that the dynamics of the arm and micro-actuator are sufficiently decoupled. This assumption is based on the fact that the micro-actuator inertia and force output are over 100 times smaller than those of the arm and thus have a minor effect on the arm dynamics. In this approach two separate SISO controllers are designed. The first

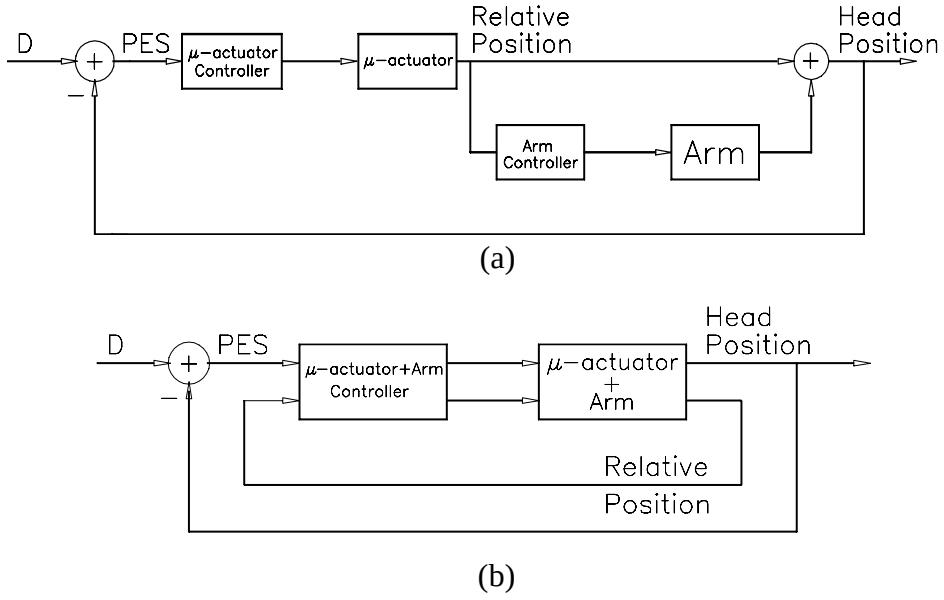


***Figure 3.1*** *Block diagram of SISO (a) and MIMO (b) controller designs. (D denotes track runout.)*

controller is designed for the arm to minimize the micro-actuator relative position. It is designed as if the controller were in a conventional disk drive, where the arm tries to minimize the PES. In this way, the full tracking capabilities of the arm can be utilized, because at the lower frequencies where the arm does maintain the micro-actuator position near zero, tracking is primarily performed by the arm. The second SISO controller for the micro-actuator accounts for the closed-loop dynamics of the arm and is designed to track the PES. The second approach is a multi-input/multi-output (MIMO) design. This approach designs a single two-input, two-output controller which takes full account of the coupling between the arm and micro-actuator. In either case, SISO or MIMO, simulations are performed using the full two-input, two-output system model. Block diagrams of each design approach are shown in Figure 3.1.

The μ-tools software uses an iterative method to design $H_\infty$ controllers satisfying the performance and uncertainty constraints included in the system description [11]. This approach is attractive for disk drive applications where the level of disturbance rejection and the bandwidth needed to achieve a desired data density is known, and the modeling uncertainty due to high frequency dynamics can be quantified. More detail about how the performance and uncertainty constraints are included in the controller specification is described below.

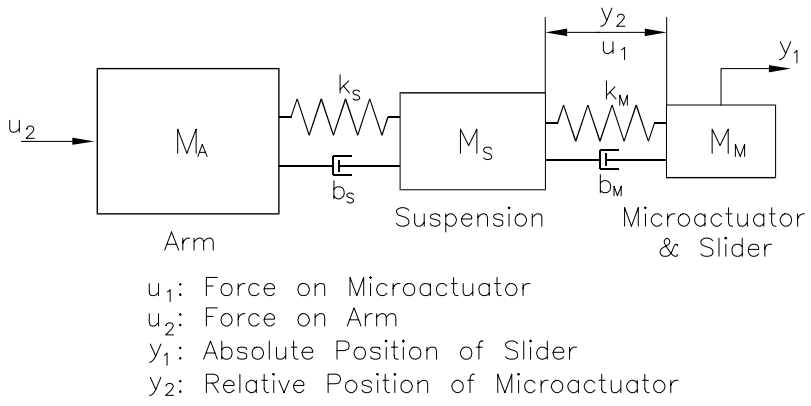


***Figure 3.2*** *Model of dual-stage disk drive used for control design.*

### 3.2.1 System Modeling

The dual-stage disk drive model used for control design and simulation is shown in Figure 3.2. A linear displacement model is shown here for simplicity. However, an analogous rotary model that more accurately represents the actual system was used for the control design. This model accounts for the system resonances which have the greatest effect on the PES and relative micro-actuator position. For the arm and suspension, the model attempts to simulate a response similar to the one shown in Figure 3.3. This is an experimentally measured plant transfer function for a commercially available disk drive and was determined using PES data. The model in Figure 3.2 captures two features of this transfer function: 1) the linear region from about 60 Hz to 2 kHz where the arm and suspension act as a pure inertia, and 2) a resonance near 2 kHz which is due to the first torsional mode of the suspension. To roughly model the effect of bearing stiction, the input to the arm was passed through a second order high pass filter with a cutoff of 60 Hz. In this way the control input to the arm is attenuated below 60 Hz, which is the approximate threshold of

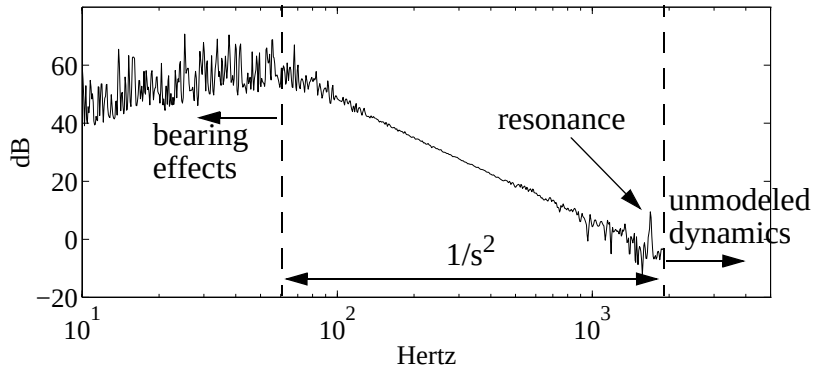


***Figure 3.3*** *Typical plant transfer function for commercial disk drive.*

bearing friction effects (see Figure 3.3). Above 2 kHz, the actual system is not well described by the model due to high frequency resonances [12]; this effect is included in the controller uncertainty specification described below. This high frequency region is not shown in Figure 3.3 because the PES sampling frequency of the disk drive limited the measurable range of the frequency response. The micro-actuator is modeled by the linearized expression given in Eq. (2.8). Although the experimental results shown in Figure 2.2 suggest that the micro-actuator is not linear over the entire ±1 μm range of motion, the linear model is used because it is expected that greater linearity can be achieved in future designs or that the micro-actuator can be linearized through feedback linearization.

The parameters used in the system model were chosen partly based on data from commercial drives and partly as design variables. For the suspension, the resonance was assumed to be at 2.0 kHz and to have a damping ratio of 0.01. The additional model parameters for the arm and suspension were based on measurements made on and specifications obtained from commercially available drives. For the micro-actuator, the resonance due to the combination of the mechanical and electrical spring stiffnesses was placed at 1.0 kHz, and the damping ratio was chosen as 0.5. The inertia included both the micro-actuator and slider, but was primarily due to the slider alone [7]. The resonance was chosen partly as a design parameter and partly based on what will be achievable in future micro-actuator designs. In general, it was chosen to be far from the intended bandwidth at 2.0 kHz and not necessarily to be the same as the resonance for the first generation design described above. Finally, the micro-actuator damping ratio of 0.05 was chosen arbitrarily. The damping is due to drag forces which act on the slider as it flies over the disk surface on an air bearing. To date no one has studied or measured the rotational or lateral dynamics of the slider relative to the suspension, making any prediction regarding damping difficult.

### 3.2.2 Controller Specifications

When used to design controllers, the μ-tools software package attempts to maintain the closed loop infinity-norm of the system below unity under a specified uncertainty restriction. In order for this process to yield meaningful controller designs, μ-tools must manipulate fictitious signals which are derived by scaling the actual inputs and outputs by frequency dependent weighting blocks; the only information known about these fictitious signals is that the infinity-norm is at most unity. The block diagram including the performance and uncertainty weighting blocks used in the control design is shown in Figure 3.4. Although the MIMO model is shown, the same weightings were also used for the SISO design.

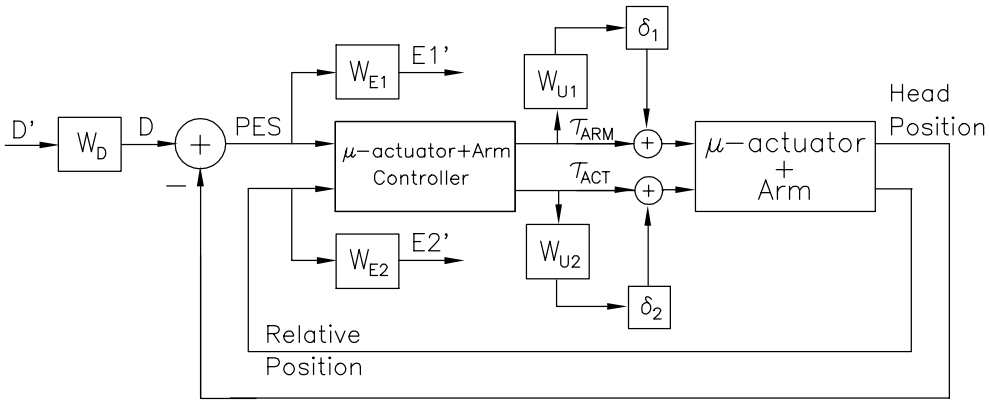


***Figure 3.4*** *μ-tools system block diagram with performance and uncertainty weighting blocks.*

The fictitious primed track runout input (*D'*) and outputs (*E1'* and *E2'*) with an infinity-norm less than unity are respectively scaled by the frequency dependent performance weights $W_D$, $W_{E1}$, and $W_{E2}$ to get the actual track runout input (*D*) and outputs (PES and micro-actuator relative position). The weightings $W_D$, $W_{E1}$, and $W_{E2}$ were chosen based on the expected and desired frequency dependence of the inputs and outputs. In general, to keep the overall system model order and resulting controller order low, weightings of at most second order were used. The second order disturbance weighting, $W_D$, used in the design is shown in Figure 3.5. The shape of this weighting was chosen because the non-repetitive track runout in the disk drive is expected to have a large low frequency component, with a steady decrease in magnitude for

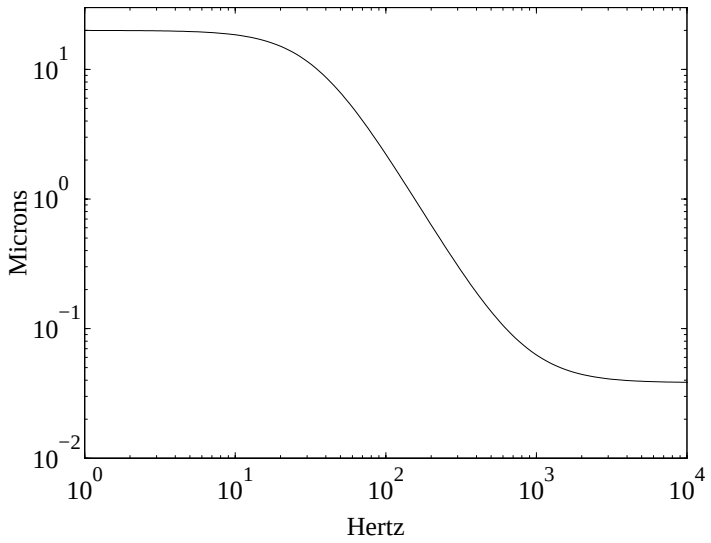


***Figure 3.5*** *Disturbance weight ($W_D$) used for μ-tools design.*

increasing frequency [12]. Thus, the spectrum of the actual track runout, $D$, is determined by the weighting function. The specific low frequency magnitude and the roll-off frequency was chosen such that when combined with $W_{E1}$ and $W_{E2}$, the low frequency disturbance attenuation is 48 dB for the PES and 32 dB for the micro-actuator position, and the bandwidth is greater than 800 Hz for the PES and greater than 225 Hz for the micro-actuator position, as discussed below. For $W_{E1}$ and $W_{E2}$ constant values were used since specific limits on the PES and micro-actuator relative position were known. To leave some room for error in the disturbance weighting specification, $W_{E1}$ divided the PES by 80 nm, and $W_{E2}$ divided the micro-actuator position by 0.5 μm.

The combination of the weightings $W_D$ and $W_{E1}$ force the closed loop PES transfer function to have a low frequency disturbance attenuation of at least 48 dB, with a bandwidth above 800 Hz. $W_D$ and $W_{E1}$ require the micro-actuator relative position to be attenuated relative to the disturbance by at least 32 dB at low frequencies, with an attenuation bandwidth greater than 225 Hz. The attenuation factors are based on the amount the low frequency runout weighting must be attenuated in order to maintain the output signals below their specified bounds, and the bandwidth specifications are based on the maximum frequency at which the runout weighting is still larger than the bound on the output. The selection of micro-actuator weights assures that below the attenuation bandwidth, primarily the arm performs tracking, and above this bandwidth, the micro-actuator tracks the disturbance. The overall micro-actuator bandwidth is then equivalent to the maximum bandwidth at which the PES is attenuated relative to the runout. For the SISO design, only the weightings $W_D$ and $W_{E2}$ were used in the arm controller design. However, for the micro-actuator controller design, all three weights were used in a similar way as for the MIMO design. Thus, as discussed above, in the dual-stage design, the arm tracking the micro-actuator position becomes analogous to the arm tracking the track runout in a conventional drive.

The performance transfer function limits were chosen based on a rough calculation from the sensitivity transfer function of a commercially available disk drive. The runout attenuation in that drive, which has a track density of 4,000 tracks per inch, is 32 dB, with a maximum runout to PES attenuation bandwidth of about 300 Hz. The same disturbance attenuation value and a somewhat more conservative bandwidth were chosen for the micro-actuator position because of the similarity in function of the arm in the single and dual-stage drives. A conservative bandwidth was chosen due to the inclusion of modeling uncertainty. For the PES, the low frequency runout attenuation in the commercial drive was scaled up by the same factor as

the track density to reach the desired density of 25,000 tracks per inch. The track runout attenuation bandwidth was specified to be a little below the desired value of 2.0 kHz, again to accommodate the model uncertainty, which will be described below. Although these tracking specifications were chosen based on a conventional drive, it should also be noted that in future designs the presence of the micro-actuator may allow the bandwidth of the arm to be decreased relative to a conventional disk drive because the micro-actuator can compensate for some of the low frequency tracking. Thus, the design requirements for the arm may be relaxed.

Modeling uncertainty for the arm and micro-actuator is used to capture the effect of unmodeled high frequency dynamics. In Figure 3.4, the uncertainty weights $W_{U1}$ and $W_{U2}$ respectively act on the arm torque ($\tau_{ARM}$) and micro-actuator torque ($\tau_{ACT}$) to produce a control input uncertainty. Similar to the performance weights, $\delta_1$ and $\delta_2$ are arbitrary gains with an infinity-norm less than unity. These are included as additional inputs to the system (similar to *D'*), and the net effect is to produce a frequency dependent percentage uncertainty on the control input.

The specific first order weights $W_{U1}$ and $W_{U2}$ used in the control design are shown in Figure 3.6. For both the arm and micro-actuator, the uncertainty starts at 5% at low frequencies, and it increases to 100% at high frequencies. In general the transition away from 5% uncertainty was chosen to occur in the neighbor-

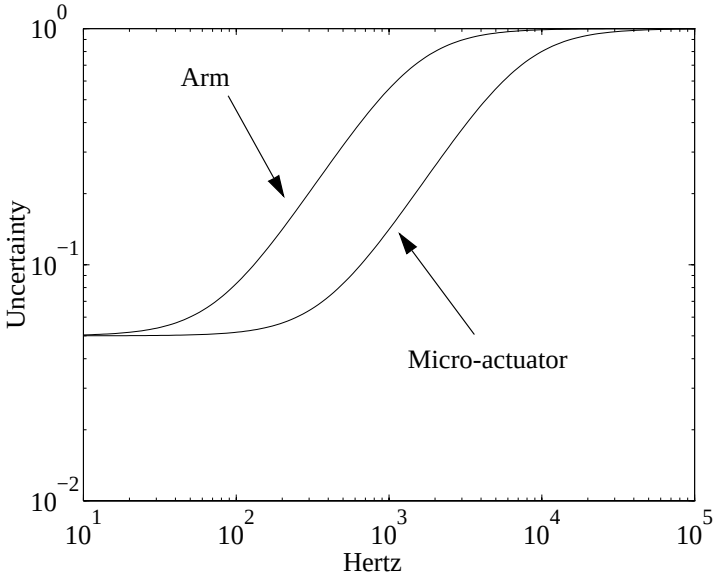


***Figure 3.6*** *Control input uncertainty used for arm ($W_{U1}$) and micro-actuator ($W_{U2}$).*

hood of the desired bandwidths for the arm and micro-actuator. Thus, both the arm and the micro-actuator are assumed to be accurately modeled up to their respective desired closed loop bandwidths. For the arm, the 20% uncertainty point is at 300 Hz, and at 2 kHz, where its first mechanical resonance is located, the uncertainty is nearly 100%. For the micro-actuator, there is 20% uncertainty at 1.5 kHz. A general rule of thumb, which was determined from the controller design obtained, is that the closed loop bandwidth of both the arm and the micro-actuator roughly corresponds to the 20% uncertainty point.

# CHAPTER 4

# Control Design Procedure

## 4.1 Overview

The software used to design the SISO and MIMO controllers with μ-tools in Matlab is discussed below. The files referenced are all included in the appendix, except for *dkit.m*, which is part of the μ-tool software. The procedure follows the general methodology discussed in Chapter 3.

## 4.2 SISO DESIGN

The SISO design utilizes two separate SISO controllers, one for the arm and one for the micro-actuator. The arm controller is designed using a single-stage disk drive model containing the arm and suspension alone. Once this controller has been designed, the loop is closed around the arm controllers using the dual-stage disk drive model (micro-actuator added to single-stage model). The input to the arm controller is the relative position of the micro-actuator, and the output is the torque on the arm. The remaining inputs and outputs are then the PES and the micro-actuator torque, and these are used when designing the micro-actuator controller.

### 4.2.1 Arm Controller Design

#### 4.2.1.1 System Definition.

The file that sets up the system for the design of the arm controller is *u_sing1.m*. This file first calls the function *mass_1.m* to create the single-stage disk drive model. The file *mass_1.m* creates a rotary model of

the arm and suspension, including some effect from low frequency friction. The parameters used are contained in the file *arm_para.m*. The basic model without friction is created using the standard state space representation, and then this is converted into the state space representation used by μ-tools using the command '*pck*' ([11], p. 8-137). To model low frequency friction in the arm, the torque on the arm is passed through a high-pass filter ($W_F$) with a cut-off of 60 Hz. A new friction-effected system is created by adding the filter to the initial model using the typical μ-tools system definition commands ([11], pp. 2-33--2-38). The final system is formed by creating a minimal realization of the system. This is necessary because the friction filter contains two zeros at the origin that cancel the two poles at the origin from the basic model. If a minimal realization is not created, numerical effects can hamper subsequent control designs.

After the system model has been created, the performance and uncertainty weights must be added before the controller can be designed. The file *weights.m* creates all of the performance and uncertainty weightings used by the SISO or MIMO designs. The performance weights used for the arm controller are $W_R$ (same as $W_D$ before) and $W_{E2}$. $W_R$ is the weight describing the expected worst-case runout in the drive, and $W_{E2}$ defines the desired limit on the PES (for the single-stage case). $W_{U1}$ is the uncertainty weighting used on the torque input to the arm. When these performance and uncertainty weights are added to the system, again using the standard μ-tools system definition commands, a three-input, three-output open loop system is created. The first input and output are used to add uncertainty, the second input and output are the normalized input and output which are used to measure performance, and the third input and output are the real variables used by the arm controller. Here, all the normalized inputs and outputs used to measure performance and uncertainty robustness have an infinity-norm less than one.

Once the system has been defined, the states are balanced to avoid numerical problems during the μ-tools design. Due to the large range of magnitudes of parameters in the system model, the initial controller design during the D-K iteration can have a very large infinity-norm, which can then lead to problems in the subsequent iterations. To minimize this effect, the nominal system ('*dual_open*') is scaled by the function *conmuscl.m* to create the balanced system '*bal_dual*'. This function scales the states of the nominal system so that the initial controller design has a reasonably small infinity norm.

The last variable defined by *u_sing1.m* is the file which defines the variables used by *dkit.m* for controller design: *problem1.m*. The variables are: the open-loop system name ('*bal_dual*' in this case), the number of

measurements used by the controller and the number of controlled variables (one for each in this case), the frequency points to use for evaluating μ, and the block matrix defining the structure of the uncertainty and performance variables. For this problem, the block matrix is '[1 1; 1 1]', meaning there is one complex uncertainty, one closed loop input, and one closed loop output ([11], pp. 4-1-4-38).

#### 4.2.1.2 Controller Design.

Once the problem definition is complete, *dkit.m* can be used to perform the controller design ([11], pp. 5-1-5-10, 4-38-4-42). *Dkit.m* first designs an H-infinity controller for the nominal system defined in *problem1.m*. The controller is designed to achieve the smallest possible infinity-norm (γ), subject to the minimum, maximum, and tolerance for γ, each of which is defined by the user or the software before the controller is designd. Using this minimum norm controller, a plot of the closed-loop singular values is shown to determine if the frequency range specified fully captures the dynamics of the system. Though the frequencies defined in *problem1.m* are used as the default, this can be modified as necessary. After the frequency points are determined, μ for the new closed loop system is calculated at those frequencies, and a plot is shown. At this point the control design can either be ended, if μ is less than one as is required for robust performance, or another iteration can be started.

If another iteration is chosen, then the *D*-scales for the next design iteration must be chosen. When calculating μ, a *D* matrix is calculated at each frequency which gives the corresponding value of μ for the closed loop system. In general, μ is bounded by:

$$\mu \leq \min \ \sigma(DMD^{-1}), \tag{4.1}$$

where the minimum is taken over the *D*-matrix, *M* is the closed loop system, and μ is calculated on a frequency by frequency basis. The process of reaching the smallest value of μ involves trying to find the optimum controller and *D*-scale which give the minimum μ. This is achieved in an iterative process: a controller is designed (*K*-iteration); the D-scale is determined for that controller to calculate μ (*D*-iteration); this new D-scale is absorbed into the nominal open loop system; a new controller is designed. Using this process, μ generally becomes progressively smaller as better and better controllers and *D*-scales are found; the process continues until a satisfactorily small μ is achieved.

In order to absorb the *D*-scale into the nominal system so a new controller can be designed, the *D*-scale must have a functional description. When calculating μ, numerical values for *D* are used at each frequency. This numerical data must be fit to a state space description so it can be added to the nominal system. When fitting the *D*-scales, there are generally several functions to fit, depending on the system. For the arm controller there are two functions: one for the uncertainty and one for the performance variables. In general it is desirable to fit these functions with as low order systems as possible because these functions add directly to the controller order for the next iteration. The last fit, that for the performance variable, must always be of order zero because it is a flat line. For the uncertainty function, however, the fit order must be chosen. While choosing the fits, a plot of μ based on the fitted *D*-scales, a plot of the curve being fit, and a plot of the sensitivity of μ to the curve fit over the range of frequencies is shown. These plots can be used to help choose an appropriate fit. In general it is desirable for the μ calculated with the fitted *D* to be fairly close to the actual μ to get good results in the subsequent control design. One option for choosing a fit is the '*apf*' command ([11], pp. 5-13-5-14), which automatically fits the *D*-scale with a function smaller than the maximum defined by the user. Though useful, this command can sometimes provide unnecessarily large order fits.

The process of designing controllers and choosing *D*-scale fits should continue until μ becomes less than one. Once this is accomplished, a suitable controller has been found that achieves robust performance and controller order reduction can be attempted if necessary. In general, if order reduction is necessary, it is advisable to have several controllers that achieve $\mu < 1$ because order reduction can be unpredictable. The maximum chance of success requires having several controllers from which to choose.

#### 4.2.1.3 Controller Order Reduction

Performing order reduction on the controllers involves finding the states of the controller with the smallest Hankel norm and attempting to remove some of these states. Testing the reduced order controllers is achieved by first ensuring that the closed-loop system with the reduced controller is still stable, and then determining if the new controller still maintains $\mu < 1$. In general, if a given reduced order controller does not satisfy either of theses constraints (stability or μ), then a higher order controller will be required. Also, because stability is a easier condition to verify, this condition should generally used as the initial criterion for reducing the order. A more detailed description of order reduction can be found in [11](pp. 3-52-3-54), but an example reduction procedure is listed below.

*[kb,hs] = sysbal(k_dk#);*
% k_dk# is nominal controller

*k_red = strunc(kb, # states);*
% k_red is new controller with the number of states specified

*clp = starp(dual_open, k_red)*;
% this creates the closed loop system

*spoles(clp);*
% check poles of *clp*; if unstable, increase controller order

*w = logspace(0,5,50);*
% create frequency points for μ evaluation

*clp_g = frsp(clp,w);*
% calculate closed loop matrix at each frequency point
% if numerical problem exist, use *[clp,hs]=sysbal(clp);*

*[bnds] = mu(clp_g, [uncertainty; performance]);*
% calculate μ of system; [unc;perf]=[1 1;1 1] for arm controller

*vplot('liv,m', bnds);*
% find peak value of μ
% if μ > 1, increase controller order
% *w* may required modification to focus in on parts of curve

### 4.2.2 Micro-Actuator Controller Design

Once the reduced order arm controller has been determined, the micro-actuator controller can be designed. The loop is closed around the arm controller in the dual-stage model, and the micro-actuator controller is designed using the PES as the control input and the micro-actuator torque as the control output.

The file that creates the open loop system for the second-stage design is *u_sing2.m*. The file used to create the dual-stage disk drive model is *mass_3.m*. This file is almost identical to *mass1.m*, except for the addition of the micro-actuator. Many of the physical parameters are taken from *system.m*, which further calls *mofi.m*, *flexure.m*, and *pplatef.m*. However, the definitions for the damping and stiffness from *system.m* are overridden by those within *mass_3.m*.

As in *u_sing1.m*, the performance and uncertainty weights are taken from *weights.m*. Now all of the

weights, $W_R$, $W_{E1}$, $W_{E2}$, $W_{U1}$, and $W_{U2}$ are used. The weights from the previous design are still included to ensure that the new closed-loop system will still satisfy the requirements. As before, $W_R$ weights the input disturbance. In the dual-stage design $W_{E1}$ is used for the PES signal, and $W_{E2}$ is used for the relative position of the micro-actuator. The uncertainty weights are again used as control input uncertainties, where $W_{U1}$ is the arm torque weight and $W_{U2}$ is the micro-actuator torque weight.

When the open loop interconnection is created, the key difference from the previous control design is that the arm controller is added. The reduced order arm controller is contained in the file *arm_red.mat*, and should have been created after the design of the arm controller was completed. The final open-loop system has a similar form to the previous design however. The first two inputs and outputs are for uncertainty, the third input and the third and fourth outputs are the normalized variables used to evaluate performance, and the last input and output are the real variables used in the control design.

The scaling performed by *conmuscl.m* is again performed for the micro-actuator controller. In this case, the uncertainty block is '[1 1; 1 1]' since there are two independent complex uncertainty terms in the dual-stage design. The variables used by *dkit.m* are defined in *problem2.m*. The open loop interconnection is again '*bal_dual*,' there is again one control measurement and one controlled variable, the frequencies are redefined to reflect the new system, and the block matrix for the structure of the uncertainty and performance is now '[1 1; 1 1; 1 2]'. Here the uncertainty is the same as mentioned previously, and the performance block is due to the one closed-loop input and two closed-loop outputs.

The remaining part of the controller design occurs almost identically to the design for the arm controller. When fitting the *D*-scales, there are three fittings due to the two uncertainty terms and the one set of performance variables. Other than this difference, the control design and controller order reduction are the same as before.

## 4.3 MIMO DESIGN

The MIMO design uses the dual stage disk-drive model to create a single two-input, two-output controller. The design process is very similar to the process for the SISO designs. The file that creates the system definition is *u_sing3.m*. This file is very similar to *u_sing2.m* except that no arm controller is added. The other

minor difference is that a small noise weight ($W_N$) is added. The noise weight is required in order to give the system the proper rank, but it is chosen to be very small to have a minimal effect on the controller design. The file used to define the variables for *dkit.m* is *problem.m*. For the MIMO design there are two measurements and two controls. The block matrix for the uncertainty and performance is '[1 1; 1 1; 2 2]'. Again there are two independent complex uncertainties, two closed-loop outputs, and now two closed-loop inputs due to the addition of the noise weight.

The remainder of the control design and order reduction proceeds identically to the micro-actuator design in the SISO case. The same performance and uncertainty weights as are used in the SISO design are used in the MIMO design (with the addition of the noise weight), and there are again three *D*-scales to fit.

# CHAPTER 5

# Control Design Results

The final, nominal closed-loop PES sensitivity transfer functions for the SISO and MIMO controllers designed based on the above specifications are shown in Figure 4.1. The nominal transfer functions representing the tracking of the track runout by the micro-actuator are shown in Figure 4.2. The single-stage controller designed for the arm alone in the SISO approach is also shown in Figure 4.1 in order to compare the dual-stage results with a single-stage system. A key feature of the PES transfer functions is that while the single-stage design flattens out at 60 Hz due to bearing friction, the micro-actuator enables the dual-stage designs to continue increasing the attenuation beyond 60 Hz, resulting in an increased low frequency attenuation of 25 dB relative to the single-stage design. The single-stage controller achieves a low frequency PES disturbance attenuation of 33 dB with a 6 state controller and a bandwidth of 400 Hz. Both the MIMO and SISO controllers have a low frequency PES disturbance attenuation of 59 dB. The MIMO controller uses only a 9 state controller and achieves a bandwidth of 3.0 kHz. The SISO design, on the other hand, requires a 13 state controller (6 for the arm and 7 for the micro-actuator), and achieves a bandwidth of 2.0 kHz. For each of the controllers, order reduction was performed by eliminating some of the states with the smallest Hankel singular values [11]. The control order for the both the MIMO and SISO designs was the minimum achievable while still maintaining robust performance. This was tested by checking that the $\mu$ of the closed loop system was still less than unity for the reduced order controllers.

As an additional measure of robustness for each of the designs, the phase and gain margins for each controller was determined. The open loop phase margin for the single-stage design is $52^{o}$, with a gain margin of 23 dB. For the MIMO and SISO designs, the margins were determined by breaking the feedback from

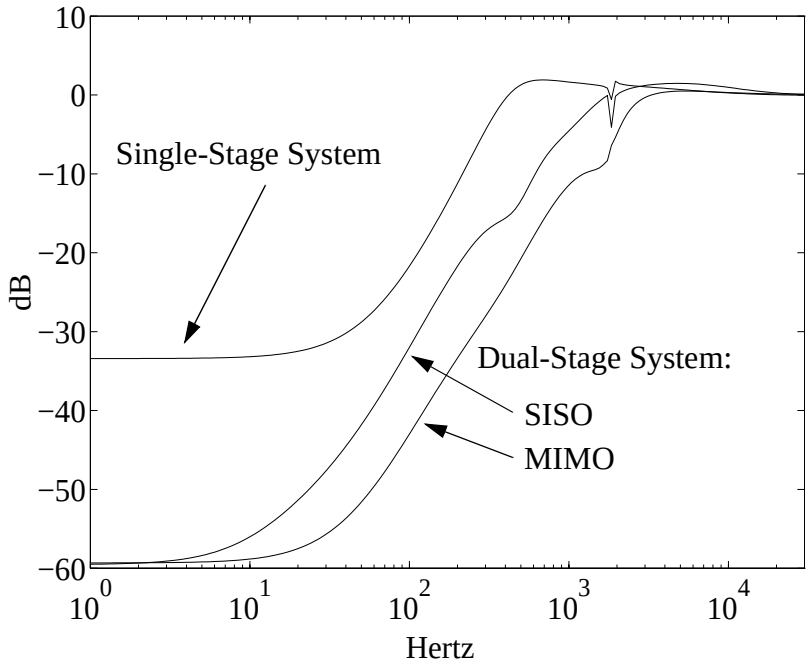


***Figure 4.1*** *Nominal closed-loop PES to disturbance transfer function for single and dual-stage controllers.*

the head position and then looking at the open loop transfer function from PES to head position. For the MIMO design, a phase margin of $60^o$ is achieved with a gain margin of 60 dB. The corresponding SISO margins are $65^o$ and 24 dB.

The micro-actuator track runout tracking is very similar in both the SISO and MIMO designs. For the SISO design, the low frequency attenuation from track runout to relative position is 33 dB, and for the MIMO design it is 37 dB. In this region, tracking is done primarily by the arm. However, in order for the dual-stage servo to achieve the full runout to PES low frequency attenuation shown in Figure 4.1, some additional tracking is performed by the micro-actuator in the low frequency region. For the both the SISO and MIMO designs, the relative position transfer function is near 0 dB from 400 Hz to the system band-widths of 2.0 kHz and 3.0 kHz, respectively. This region represents the frequencies over which tracking is done primarily by the micro-actuator since in this frequency region the relative position is approximately equal to the track runout.

A final feature of both the PES and micro-actuator position transfer functions is the small notch that occurs

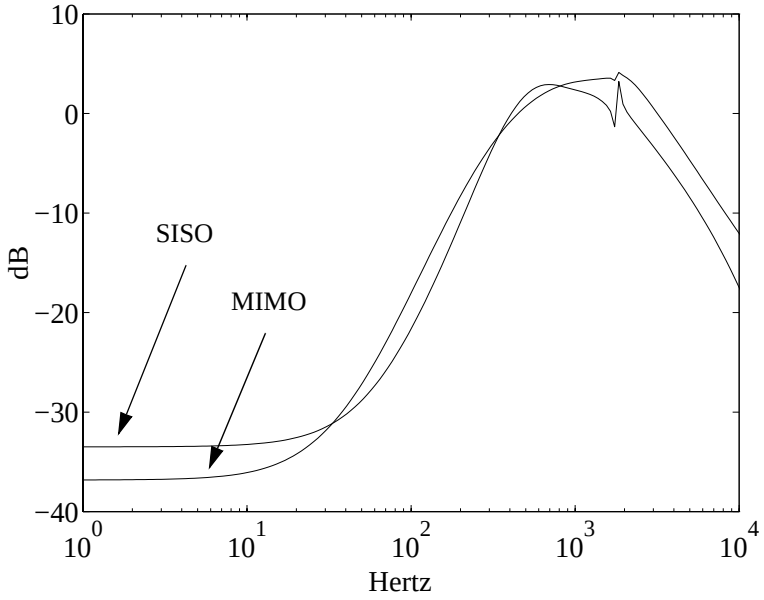


***Figure 4.2*** *Micro-actuator relative position to disturbance transfer function for SISO and MIMO designs.*

at the suspension resonance. Although it is more significant in the SISO design, it occurs to some extent in both designs. This is due to the fact that the controller attempts to cancel the resonance, but cannot do so perfectly due to the model uncertainty. As a result, some residual effect is seen in the nominal transfer function. Nevertheless, over the specified range of uncertainty, the μ-tools design guarantees that the system will remain stable and achieve the performance specifications.

# CHAPTER 6

# Conclusions

The first generation micro-actuator designed and tested by David Horsley has been shown to be capable of nearly achieving the desired 2.0 kHz bandwidth with a range of motion of ±1 μm. Though this initial parallel plate design does not have much force non-linearity over the desired range of motion, it is expected that this effect will only worsen in future designs. For this reason, electrostatic simulations were perfomed for actuators driven by comb fingers. Comb fingers are expected to have a force independent of displacement and thus no non-linearity. Though the simulation did contain a linear range of operation, the results also showed that for certain geometries and under certain operating conditions significant non-linear effects appear. Hopefullly these results can therefore be used as a design guideline for selecting comb finger geometries that avoid the non-linear range of operation.

Two control design methodologies for the dual-stage disk drive were shown to meet desired performance and uncertainty specifications. The inclusion of uncertainty robustness is important not only for the presence of unmodeled dynamics, but also due to the varying operating conditions encountered by a disk drive. The simulated performance of the MIMO controller provided a higher bandwidth with a smaller order controller than did the SISO controller. However, no generalization is made in this respect because the μ-tools design methodology is only guaranteed to meet the minimum specified performance and uncertainty, and controller order reduction can be an unpredictable process. The smaller order and higher bandwidth of the MIMO design appear to make it more attractive than the SISO design in this case. However, the final choice will depend on the precise performance levels desired and whether each design can meet those specification. Furthermore, implementation on a disk drive is an important consideration because the SISO

controller may potentially be incorporated as an add-on compensator in a conventional servo system, whereas the MIMO design will require a completely new servo architecture.

# REFERENCES


1. E. Grochowski and R.F. Hoyt, “Future Trends in Hard Disk Drives,” *IEEE Trans. Magnetics*, vol. 32, no. 3, pp. 1850-1854, 1996.

2. L.-S. Fan, H.H. Ottesen, T.C. Reiley, and R.W. Wood, “Magnetic Recording-Head Positioning at Very High Track Densities Using a Microactuator-Based, Two-Stage Servo System,” *IEEE Trans. Ind. Electronics*, vol. 42, no. 3, pp. 222-233, 1995.

3. K. Akagi, H. Otsuki, T. Yamaguchi., and K. Mori, “Servo signal quality and dual-stage actuator system for micron trackwidth,” *Journal of Magnetism and Magnetic Materials*, vol. 134, pp. 242-247, 1994.

4. P. Cheung, R. Horowitz, and R.T. Howe, “Modeling and Position Detection of a Polysilicon Linear Microactuator,” *Micromechanical Sensors, Actuators and Systems, Proceedings of the 1991 ASME Winter Annual Meeting*, vol. DSC-32, pp. 269-278, December, 1991, Atlanta, GA.

5. K. Takaishi, T. Imamura, Y. Mizoshita, S. Hasegawa, T. Ueno, and T. Yamada, “Microactuator Control for Disk Drive,” *IEEE Trans. Magnetics*, vol. 32, no. 3, pp. 1863-1866, 1996.

6. P. Cheung, R. Horowitz, and R.T. Howe, “Design, Fabrication, Position Sensing, and Control of an Electrostatically-Driven Polysilicon Microactuator,” *IEEE Trans. Magnetics*, vol. 32, no. 1, pp. 122-128, 1996.

7. D.A. Horsley, A. Singh, A.P. Pisano, and R. Horowitz, “Angular Micropositioners for Disk Drives,” *Intl. Workshop on Micro Electro Mechanical Systems*, Nagoya, Japan, pp. 454-459, 1997.

8. T. Hirano, L.-S. Fan, and J.Q. Gao, “Invar MEMS Milliactuator for Hard Disk Drive Applications.” *Intl. Workshop on Micro Electro Mechanical Systems*, Nagoya, Japan, pp. 378-382, 1997.

9. C.G. Keller and M. Ferrari, “Milli-Scale Polysilicon Structures,” *Solid-State Sensor and Actuator Workshop*, Hilton Head SC, pp. 132-137, June 1994

10. A. Singh, D.A. Horsley, M.B. Cohn, A.P. Pisano, and R.T. Howe, “Batch Transfer of Microstructures using Flip-Chip Solder Bump Bonding,” to appear in the *9th Annual Intl. Conference on Sensors and Actuators (Transducers ‘97)*, June 1997.

11. G.J. Balas, J.C. Doyle, K. Glover, A. Packard, and R. Smith, μ-*Analysis and Synthesis Toolbox*, MUSYN and Mathworks Inc., 1995.

12. J.-Y. Yen, K. Hallamasek, and R. Horowitz, “Track-Following Controller Design for a Compound Disk Drive Actuator,” *Journal of Dynamic Systems, Measurement, and Control*, vol. 112, pp. 391-402, September 1990.